

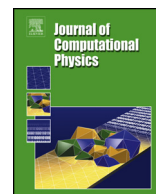


ELSEVIER

Contents lists available at ScienceDirect

Journal of Computational Physics

www.elsevier.com/locate/jcp



A mass-conserving axisymmetric multiphase lattice Boltzmann method and its application in simulation of bubble rising

Haibo Huang^{a,*}, Jun-Jie Huang^b, Xi-Yun Lu^a^a Dept. of Modern Mechanics, Univ. of Sci. and Tech. of China, Hefei, 230026, China^b Dept. of Engineering Mechanics, Chongqing University, Chongqing, 400044, China

ARTICLE INFO

Article history:

Received 24 September 2013

Received in revised form 14 March 2014

Accepted 20 March 2014

Available online 26 March 2014

Keywords:

Lattice Boltzmann

Multiphase

Axisymmetric

Bubble rising

Mass conservation

ABSTRACT

In many lattice Boltzmann studies about bubble rising, mass conservation is not satisfactory and the terminal bubble rising shape or velocity is not so consistent with experimental data as those obtained through other CFD techniques. In this paper, based on the multiphase model (He et al., 1999 [1]), a mass-conserving axisymmetric multiphase lattice Boltzmann model is developed. In the model, a mass correction step and an effective surface tension formula are introduced into the model. We demonstrate how the macroscopic axisymmetric Cahn–Hilliard equation and Navier–Stokes equation are recovered from the lattice Boltzmann equations through Chapman–Enskog expansion. The developed model is applied to simulate the bubble rising in viscous fluid. The mass correction step in our scheme significantly improves the bubble mass conservation. The surface tension calculation successfully predicts the terminal bubble shapes and reproduces the effect of initial bubble shape. The terminal bubble rising velocities are very consistent with experimental and numerical data in the literature. Qualitatively, the wakes behind the bubbles also agree well with experimental data. This model is useful for predicting the axisymmetric two-phase flows.

© 2014 Elsevier Inc. All rights reserved.

1. Introduction

Lattice Boltzmann method (LBM) has been developed into a powerful tool to simulate multiphase flows [1–5]. The LBM has many advantages compared to the common computational fluid dynamics (CFD) method. First it is based on the molecular kinematic theory [6], it is able to recover macroscopic Navier–Stokes (NS) equation. Second, usually it involves an equation of state. Hence, it is not necessary to solve Poisson equation in the LBM, which may take much effort in the common CFD. Third it is an explicit scheme and easy to be parallelized.

There are several popular multiphase LBM models. The first one is the color-gradient model proposed by Gunstensen et al. [7], which is based on the Rothman–Keller (R–K) lattice gas model [8]. Usually, the color-gradient model is used to simulate binary fluid flows with identical densities [9].

The second type is the Shan–Chen (S–C) model [10]. The S–C single component multiphase model seems working well with high density ratios [11]. Recent study shows that the surface tension and the ratios of densities and viscosities also can be adjusted independently [12]. This finding may expand the application of the S–C model. However, our recent study [13] shows there is a defect in the forcing strategy on the S–C model. Through a correct forcing strategy, the S–C model

* Corresponding author.

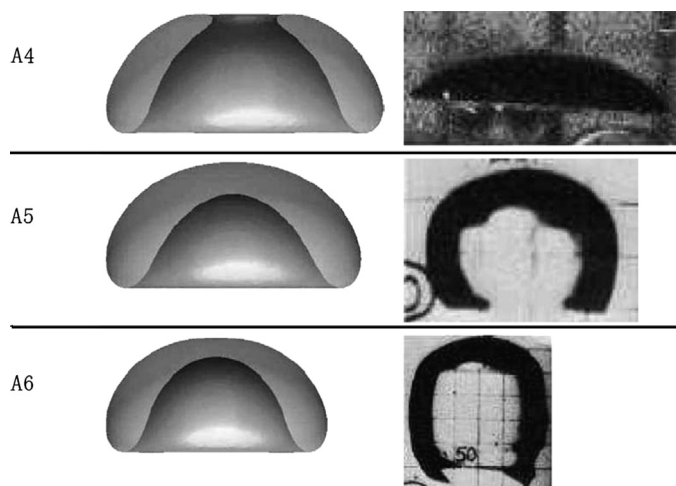


Fig. 1. Comparison of LBM result (Amaya-Bower and Lee [4], the left column) and experimental data [22] (the right column). The figure is copied from the Table 2 in Ref. [4]. The Eötvös number and Morton number of cases A4, A5, and A6 (upper, middle, and lower rows) are illustrated in Table 1.

can achieve the maximum density ratio about 300 for 2D simple cases about a liquid droplet immersed inside a vapor phase. Sankaranarayanan et al. [14] and Gupta and Kumar [15] used the S–C model to study the bubble rising. However, in both studies the parameters are limited to a very narrow range. Besides that, in the 2D study of Gupta and Kumar [15], the comparison between the LBM simulation and experimental data is poor in terms of bubble shape. Srivastava et al. [16] developed the Shan–Chen multiphase model for axisymmetric flows. However, no complex flow phenomena, e.g., bubble rising, were tested and the mass conservation issue is unknown.

The third type is the free energy (FE) LBM [17]. The original FE model [17] is known as not Galilean invariant for the viscous terms in the Navier–Stokes equation [6,17]. Inamuro et al. [18] achieved a high density ratio through improving Swift’s free-energy model [17], but the model has to solve a Poisson equation, which decreased the simplicity of the LBM. Frank et al. using the LBM simulated the bubble rising [19]. However, only cases with very small Reynolds number were simulated and the corresponding terminal spherical and oblate ellipsoidal bubbles were observed [19]. Cheng et al. [20] using a free energy based model [21] studied 3D bubble–bubble interactions. However, because the model [21] they used is not able to include the density contrast effect, the result is only limited to density match cases.

Later He et al. [1] proposed an incompressible multiphase LBM, which is referred to as HCZ model. In the model, one set of distribution function is used to recover the incompressible condition and NS equations. The other set of distribution function is able to recover a macroscopic Cahn–Hilliard (CH) equation, which is usually used to track the interfaces between different phases. Recently, a series models [2,4,5] based on the model of He et al. [1] have been further developed to handle higher density-ratio multiphase flow, which is referred to as Lee–Lin models. These models seem to be able to simulate density ratio as high as 1000 [2,4]. For cases of a droplet splashing on a thin liquid film, the result looks good compared with some experiment data [2]. The parameter-study about bubble rising [4] is much wider than the other corresponding LBM studies.

However, in terms of terminal bubble shape, the result of Amaya-Bower and Lee [4] has large discrepancy with the experimental data. For example, Fig. 1 shows some comparison in Table 2 in Ref. [4]. For case A4, the shape of the bubble is spherical cap in the experiment [22]. However, the simulated result is a toroidal bubble, which is very different from the spherical cap bubble. They attributed the discrepancy to grid resolution [4]. But it is difficult to explain why the aspect ratio of the toroidal is very different from the experimental one. For the cases A5 and A6, basically the terminal bubble shapes are skirted with rounded lower edge. However, for cases with high Re , the rounded lower edge should become sharper (refer to Fig. 8). In a word, in terms of bubble shape, some simulation results with Lee–Lin model are not consistent with the experimental ones.

Although some other studies based on the HCZ model or Lee–Lin model to handle the axisymmetric two-phase flows are carried out [23–25], the validation cases are mainly focussed on very simple droplet flow problems, for example, droplet oscillation and droplet collision. In the following Section 3, we will show the poor comparison between the simulations using these models [24] and the experimental one. Besides, the issue of mass conservation is unknown [23–25]. Actually, in terms of mass conservation, the original HCZ model is not satisfactory [26]. Because these models (including the Lee–Lin model) are based on the HCZ model, the mass conservation property may be not so satisfactory for bubble rising [4].

Here based on the HCZ model and a technique to ensure mass conservation, an axisymmetric HCZ model is developed to simulate the bubble rising problem. The mass conservation is ensured through a mass correction step in the simulation. The revised surface tension calculation is shown more superior than the original surface tension calculation in the HCZ model. All typical bubble shapes in experiment [22] are observed and compared in detail. The effect of initial bubble shape in the literature is reproduced correctly using our model.

This paper is organized as follows. First the macroscopic governing equation of our developed scheme is illustrated. Then the axisymmetric multiphase LBM is introduced. Finally, the scheme is used to simulate the bubble rising and compared with the experimental data and the other numerical results in the literature in detail.

2. Methods

2.1. Macroscopic governing equations

The HCZ model is an index-function based multiphase model. The governing equation for the index function ϕ in the axisymmetric coordinates (x, r -coordinates) is

$$\partial_t \phi + \partial_\beta (\phi u_\beta) + \frac{\phi u_r}{r} = \lambda \partial_\beta (\partial_\beta (p_{th} - c_s^2 \phi)). \quad (1)$$

It is a Cahn–Hilliard equation for tracking the interface and λ is the mobility (refer to Appendix A.4). x, r are the axis and radial directions, respectively. The subscript β and the following α denote Cartesian components and Einstein summation convention is applied in this paper. p_{th} is the thermodynamic pressure calculated from the Carnahan–Starling equation of state [1].

$$p_{th} = \phi RT \frac{1 + b\phi/4 + (b\phi/4)^2 - (b\phi/4)^3}{(1 - b\phi/4)^3} - a\phi^2, \quad (2)$$

where a is related to the intermolecular pairwise potential and b is the repulsion parameter or the effective molecular volume.

For the incompressible multiphase flow, the continuity equation is

$$\partial_t \rho + \partial_\beta (\rho u_\beta) = -\frac{\rho u_r}{r}. \quad (3)$$

The momentum governing equation (Navier–Stokes (N–S) equation) is:

$$\rho \partial_t u_\alpha + \rho \partial_\beta (u_\beta u_\alpha) = -\partial_\alpha p + \partial_\alpha [\mu (\partial_\alpha u_\beta + \partial_\beta u_\alpha)] + H_\alpha + (F_s)_\alpha + G_\alpha, \quad (4)$$

where $(F_s)_\alpha$ is the “ α ”-component of surface tension \mathbf{F}_s . $\mathbf{G}(\mathbf{x}) = -(\rho(\mathbf{x}) - \rho_l)\mathbf{g}$ is the buoyant force acting on the bubble, where \mathbf{x} represents position of a computational node in the simulated domain.

Compared to purely 2D cases, there are some source terms due to axisymmetric effect on the right hand side (RHS) of the N–S equation, i.e.,

$$H_\alpha = \mu \left\{ \frac{\partial_r u_\alpha}{r} - \frac{u_r}{r^2} \delta_{\alpha r} + \partial_\alpha \left(\frac{u_r}{r} \right) \right\} - \rho \frac{u_r u_\alpha}{r}. \quad (5)$$

In the above expression, μ is the dynamic viscosity. Here all the source terms in the N–S equation are integrated as $\mathbf{F} = \mathbf{H} + \mathbf{F}_s + \mathbf{G}$.

For the 2D cases, the surface tension \mathbf{F}_s can be expressed in different forms [27], for example, in the study of He et al. [1]

$$\mathbf{F}_s = \kappa \rho \nabla (\nabla^2 \rho), \quad (6)$$

where κ is the surface tension coefficient. This is referred to as “original” surface tension calculation.

However, the above original surface tension calculation in the HCZ model changes its direction across the bubble interface, and a wiggle over the interface region would appear [26]. The wiggle may cause numerical instability at large density ratio. Some study [26,27] demonstrated that the following “revised” surface tension calculation is better.

$$\mathbf{F}_s = -k \nabla \cdot \left(\frac{\mathbf{n}}{|\mathbf{n}|} \right) |\nabla \phi| \nabla \phi, \quad (7)$$

where the normal vector \mathbf{n} is defined to be $\mathbf{n} \equiv \nabla \phi$.

For the axisymmetric cases, there is an extra terms in \mathbf{F}_s , that is

$$\mathbf{F}_s = -k \nabla \cdot \left(\frac{\nabla \phi}{|\nabla \phi|} \right) |\nabla \phi| \nabla \phi - k \frac{\partial_r \phi}{r} \cdot \nabla \phi. \quad (8)$$

In Section 2.3, we will discuss how to evaluate the terms in Eq. (8) using finite difference approximation.

In the following, our axisymmetric model based on He et al. [1] will be introduced in detail.

2.2. Axisymmetric multiphase HCZ LBM

Our axisymmetric multiphase LBM is based on HCZ model [1], in which the index function ϕ is used to track interfaces between liquid and gas. In the model, two distribution functions \bar{f}_i and \bar{g}_i are introduced, which are able to recover the Cahn–Hilliard equation (evolution of the index function) and Navier–Stokes equation, respectively.

$$\bar{g}_i(\mathbf{x} + \mathbf{e}_i\delta t, t + \delta t) = \bar{g}_i(\mathbf{x}, t) - \frac{1}{\tau_1}(\bar{g}_i(\mathbf{x}, t) - \bar{g}_i^{eq}(\mathbf{x}, t)) + S_i(\mathbf{x}, t)\delta t, \tag{9}$$

$$\bar{f}_i(\mathbf{x} + \mathbf{e}_i\delta t, t + \delta t) = \bar{f}_i(\mathbf{x}, t) - \frac{1}{\tau_2}(\bar{f}_i(\mathbf{x}, t) - \bar{f}_i^{eq}(\mathbf{x}, t)) + S'_i(\mathbf{x}, t)\delta t, \tag{10}$$

where $f_i(\mathbf{x}, t)$ is the density distribution function in the i th velocity direction at position \mathbf{x} on time step t . τ_1 is a relaxation time which is related to the kinematic viscosity as $\nu = c_s^2(\tau_1 - 0.5)\delta t$. τ_2 is related to mobility $\lambda = \frac{1}{2}(1 - \frac{1}{2\tau_2})\delta t$ (refer to Appendix A.4).

Here the kinematic viscosities for the liquid ($\nu_l = c_s^2(\tau_l - 0.5)\delta t$) and gas ($\nu_g = c_s^2(\tau_g - 0.5)\delta t$) can be adjusted independently. In the pure liquid and gas area, $\tau_1 = \tau_l$ and $\tau_1 = \tau_g$, respectively. For the interfacial region, $\tau_1(\mathbf{x})$ is interpolated through

$$\tau_1(\mathbf{x}) = \tau_g + (\phi(\mathbf{x}) - \phi_g) \frac{\tau_l - \tau_g}{\phi_l - \phi_g}. \tag{11}$$

$S_i(\mathbf{x}, t)$, $S'_i(\mathbf{x}, t)$ are the source terms in Eqs. (9) and (10), respectively. The equilibrium distribution functions $\bar{g}_i^{eq}(\mathbf{x}, t)$ and $\bar{f}_i^{eq}(\mathbf{x}, t)$ can be calculated as [1]

$$\bar{g}_i^{eq}(\mathbf{x}, t) = w_i \left[p_h + \rho c_s^2 \left(\frac{e_{i\alpha} u_\alpha}{c_s^2} + \frac{e_{i\alpha} u_\alpha e_{i\beta} u_\beta}{2c_s^4} - \frac{u_\alpha u_\alpha}{2c_s^2} \right) \right], \tag{12}$$

and

$$\bar{f}_i^{eq}(\mathbf{x}, t) = w_i \phi \left[1 + \frac{e_{i\alpha} u_\alpha}{c_s^2} + \frac{e_{i\alpha} u_\alpha e_{i\beta} u_\beta}{2c_s^4} - \frac{u_\alpha u_\alpha}{2c_s^2} \right], \tag{13}$$

respectively, where p_h and ρ are the hydrodynamic pressure and density of the fluid, respectively.

In Eqs. (9) and (10), the \mathbf{e}_i 's are the discrete velocities. For the D2Q9 model, they are given by $(e_{ix}, e_{iy}) = (0, 0)$ ($i = 0$), $(e_{ix}, e_{iy}) = c(\cos(\frac{(i-1)\pi}{2}), \sin(\frac{(i-1)\pi}{2}))$ ($i = 1, 2, 3, 4$), and $(e_{ix}, e_{iy}) = \sqrt{2}c(\cos(\frac{(i-5)\pi}{2} + \frac{\pi}{4}), \sin(\frac{(i-5)\pi}{2} + \frac{\pi}{4}))$ ($i = 5, 6, 7, 8$).

In Eq. (13), for the D2Q9 model, $w_i = 4/9$ ($i = 0$), $w_i = 1/9$ ($i = 1, 2, 3, 4$), $w_i = 1/36$ ($i = 5, 6, 7, 8$), $c_s = \frac{c}{\sqrt{3}}$, where $c = \frac{\delta x}{\delta t}$ is the ratio of lattice spacing δx and time step δt . Here, we define 1 lattice unit (δx) as 1 lu and 1 time step (δt) as 1 ts.

The hydrodynamic pressure and the momentums are obtained through

$$p_h = \sum \bar{g}_i + \frac{1}{2} u_\beta E_\beta \delta t - \frac{1}{2} c_s^2 \rho \frac{u_r}{r} \delta t, \tag{14}$$

where $E_\beta = -\partial_\beta[\psi(\rho)]$ and $\psi(\rho) = p_h - c_s^2 \rho$;

$$\rho c_s^2 u_\alpha = \sum \bar{g}_i e_{i\alpha} + \frac{1}{2} c_s^2 F_\alpha \delta t. \tag{15}$$

The index function is calculated from

$$\phi = \sum \bar{f}_i - \frac{\phi}{2} \frac{u_r}{r}. \tag{16}$$

After ϕ is known, the corresponding density of the fluid can be calculated from

$$\rho = \rho_g + (\phi - \phi_g) \frac{\rho_l - \rho_g}{\phi_l - \phi_g}, \tag{17}$$

where ϕ_g and ϕ_l are the two coexistence ‘density’ of the gas and liquid, respectively in Eq. (2). In Eq. (2), $b = 4$, $a = 4 \text{ lu}^2/\text{ts}^2$, and $RT = c_s^2$ are adopted [1]. For this parameter choice, through Maxwell construction, we know that two phases with $\phi_g = 0.021$ and $\phi_l = 0.247$ would coexist.

The source terms including the axisymmetric effect and surface tension that appear in Eqs. (9) and (10) are

$$S_i = \left(1 - \frac{1}{2\tau_1} \right) \left\{ (e_{i\alpha} - u_\alpha) F_\alpha \Gamma_i(\mathbf{u}) + (e_{i\alpha} - u_\alpha) E_\alpha [\Gamma_i(\mathbf{u}) - \Gamma_i(0)] - w_i c_s^2 \frac{\rho u_r}{r} \right\}, \tag{18}$$

where $\Gamma_i(\mathbf{u}) = \bar{f}_i^{eq}/\rho$, and

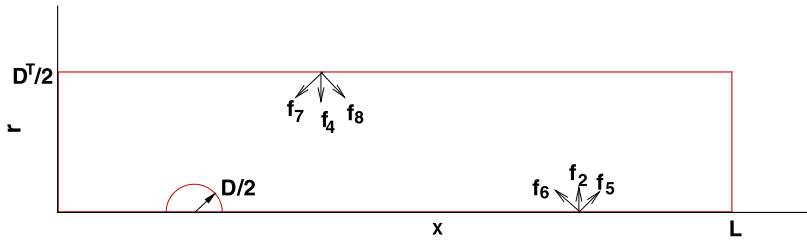


Fig. 2. Geometry of computational domain $L \times \frac{D^T}{2}$ in the (x, r) -coordinates. $r = 0$ is the axisymmetric axis.

$$S'_i = \left(1 - \frac{1}{2\tau_2}\right) \left\{ \frac{(e_{i\alpha} - u_\alpha)F'_\alpha}{c_s^2} \Gamma_i(\mathbf{u}) - w_i \frac{\phi u_r}{r} \right\}, \tag{19}$$

where $F'_\alpha = -\partial_\alpha[\psi(\phi)]$ and the function $\psi(\phi) = p_{th} - c_s^2\phi$.

Basically, the above formulae are similar to those in Ref. [24], except there are some typos in the study [24]. The major typos are: a term $-\mu \frac{u_r}{r}$ is missing in the RHS of Eq. (2) in Ref. [24], the viscous term in RHS of both Eqs. (16) and (55) in Ref. [24] should be $\mu \{ \frac{\partial u_\alpha}{r} - \frac{u_r}{r} \delta_{\alpha r} + \partial_\alpha (\frac{u_r}{r}) \}$ while not $\frac{\mu}{r} [\partial_r u_i + \partial_i u_r]$. The detailed derivations of macroscopic governing equations are illustrated in Appendices A and B.

2.2.1. MRT collision

In higher Re cases, for example, $Re > 50$, smaller τ_1 is preferred. However, if the above BGK (‘Bhatnagar–Gross–Krook’) collision is used, numerical simulation may become unstable. Here, the Multiple Relaxation Time (MRT) collision model [25, 28] is used in these simulations.

The collision terms $-\frac{1}{\tau_1}(\bar{g}_i - \bar{g}_i^{eq})$ and $-\frac{1}{\tau_2}(\bar{f}_i - \bar{f}_i^{eq})$ in Eqs. (9) and (10) should be replaced by the MRT collision model [25]. That is,

$$\bar{g}_i(\mathbf{x} + \mathbf{e}_i \delta t, t + \delta t) = \bar{g}_i(\mathbf{x}, t) - \sum_j \bar{\mathbf{S}}_{1ij}(\bar{g}_j - \bar{g}_j^{eq}) + Q_i \delta t - \frac{\delta t}{2} \sum_j \bar{\mathbf{S}}_{1ij} Q_j, \tag{20}$$

where $\bar{\mathbf{S}}_1 = \mathbf{M}^{-1} \hat{\mathbf{S}}_1 \mathbf{M}$, $Q_i = S_i / (1 - \frac{1}{2\tau_1})$.

$$\bar{f}_i(\mathbf{x} + \mathbf{e}_i \delta t, t + \delta t) = \bar{f}_i(\mathbf{x}, t) - \sum_j \bar{\mathbf{S}}_{2ij}(\bar{f}_j - \bar{f}_j^{eq}) + Q'_i \delta t - \frac{\delta t}{2} \sum_j \bar{\mathbf{S}}_{2ij} Q'_j, \tag{21}$$

where $\bar{\mathbf{S}}_2 = \mathbf{M}^{-1} \hat{\mathbf{S}}_2 \mathbf{M}$, and $Q'_i = S'_i / (1 - \frac{1}{2\tau_2})$.

The matrix \mathbf{M} is illustrated in Appendix C. The diagonal collision matrix $\hat{\mathbf{S}}$ is given by [28] $\hat{\mathbf{S}} \equiv \text{diag}(s_0, s_1, s_2, s_3, s_4, s_5, s_6, s_7, s_8)$. The parameters are chosen as: $s_0 = s_3 = s_5 = 1.0$, $s_1 = 1.64$, $s_2 = 1.54$, $s_4 = s_6 = 1.7$, and $s_7 = s_8 = \frac{1}{\tau}$. In the collision matrices $\hat{\mathbf{S}}_1$ and $\hat{\mathbf{S}}_2$, s_0 to s_6 are identical to those illustrated in the above except $s_7 = s_8 = \frac{1}{\tau_1}$ in $\hat{\mathbf{S}}_1$ and $s_7 = s_8 = \frac{1}{\tau_2}$ in $\hat{\mathbf{S}}_2$.

2.3. Calculation of the surface tension

The discretized form of Eq. (8) is illustrated in the following in detail. Fig. 2 shows the computational domain and the size is $L \times \frac{D^T}{2}$, where L is the length in axisymmetric axis direction, i.e., x -axis, and $\frac{D^T}{2}$ is the radius of the circular tube where the viscous fluid is inside. Initially a stationary bubble with diameter D is set close to $x = 0$ (the ‘‘bottom’’ of the tube). The computational domain is partitioned into a uniform Cartesian mesh with the mesh space δx . Suppose the center of each cell, $\Omega_{i,j}$, is located at $(x_i, r_j) = ((i - 0.5)\delta x, (j - 0.5)\delta x)$. The cell vertices are located at $(x_{i+\frac{1}{2}}, r_{j+\frac{1}{2}}) = (i\delta x, j\delta x)$.

The discretized form of Eq. (8) can be written as

$$\mathbf{F}_s = -k \nabla_d \cdot \left(\frac{\nabla \phi}{|\nabla \phi|} \right)_{ij} |\nabla_d \phi_{ij}| \nabla_d \phi_{ij} - k \frac{\partial_r \phi}{r} \cdot \nabla_d \phi_{ij}, \tag{22}$$

where ∇_d is a finite difference approximation to the divergence operator.

The normal vector at a vortex can be obtained by differentiating the phase field in the centers of the four surrounding cells [27]. For example, the normal vector $\mathbf{n}_{i+\frac{1}{2}, j+\frac{1}{2}} \equiv (\nabla \phi)_{i+\frac{1}{2}, j+\frac{1}{2}}$ at the top right vertex of cell $\Omega_{i,j}$ is

$$\mathbf{n}_{i+\frac{1}{2}, j+\frac{1}{2}} = \left(n_{i+\frac{1}{2}, j+\frac{1}{2}}^x, n_{i+\frac{1}{2}, j+\frac{1}{2}}^r \right) = \left(\frac{\phi_{i+1,j} + \phi_{i+1,j+1} - \phi_{i,j} - \phi_{i,j+1}}{2\delta x}, \frac{\phi_{i,j+1} + \phi_{i+1,j+1} - \phi_{i,j} - \phi_{i+1,j}}{2\delta x} \right). \tag{23}$$

The curvature of the interface $s(\phi_{i,j})$ at a cell center (i, j) is calculated from the above vertex-centered normals:

$$\begin{aligned}
 s(\phi_{i,j}) &= \nabla_d \cdot \left(\frac{\mathbf{n}}{|\mathbf{n}|} \right)_{i,j} \\
 &= \frac{1}{2\delta x} \left(\frac{n_{i+\frac{1}{2},j+\frac{1}{2}}^x + n_{i+\frac{1}{2},j+\frac{1}{2}}^r}{|\mathbf{n}_{i+\frac{1}{2},j+\frac{1}{2}}|} + \frac{n_{i+\frac{1}{2},j-\frac{1}{2}}^x - n_{i+\frac{1}{2},j-\frac{1}{2}}^r}{|\mathbf{n}_{i+\frac{1}{2},j-\frac{1}{2}}|} - \frac{n_{i-\frac{1}{2},j+\frac{1}{2}}^x - n_{i-\frac{1}{2},j+\frac{1}{2}}^r}{|\mathbf{n}_{i-\frac{1}{2},j+\frac{1}{2}}|} - \frac{n_{i-\frac{1}{2},j-\frac{1}{2}}^x + n_{i-\frac{1}{2},j-\frac{1}{2}}^r}{|\mathbf{n}_{i-\frac{1}{2},j-\frac{1}{2}}|} \right). \tag{24}
 \end{aligned}$$

The cell-centered normal is the average of vertex normals,

$$\nabla_d \phi_{ij} = \frac{\mathbf{n}_{i+\frac{1}{2},j+\frac{1}{2}} + \mathbf{n}_{i+\frac{1}{2},j-\frac{1}{2}} + \mathbf{n}_{i-\frac{1}{2},j+\frac{1}{2}} + \mathbf{n}_{i-\frac{1}{2},j-\frac{1}{2}}}{4}. \tag{25}$$

2.4. Mass correction

In the original HZC model without mass correction, the mass of a rising bubble may increase with time [26]. The possible reason is that the term on the RHS of Eq. (1) may not be negligible small near the interface [26]. In our axisymmetric model based on the HZC model, the similar unfavorable behavior in bubble rising is also observed.

Hence, the mass correction step is necessary to ensure the mass conservation in our LB simulations. In our simulations, the volume of the bubble is corrected using the scheme of Son [29],

$$\frac{\partial \phi}{\partial \tau_3} = (V - V_0) |\nabla \phi|, \tag{26}$$

where V is the bubble volume before the correction. $V_0 = \frac{1}{6}\pi D^3$ is the initial volume of the bubble, where D is the initial diameter of the bubble. τ_3 is an artificial time. The equation is computed after each streaming step till the steady state $V = V_0$ is reached.

In the implementation, V is determined in the following way. For a computational node \mathbf{x} , if $\rho(\mathbf{x}) < \frac{\rho_l + \rho_g}{2}$, it is supposed to be occupied by gas, and it is labeled as \mathbf{x}_g . The formula about calculation of the volume (integration scheme) is

$$V = \sum_{\mathbf{x}_g} 2\pi r \delta r \delta x, \tag{27}$$

where $\delta x = \delta r = 1$ lu, and r is the radius from \mathbf{x}_g to $r = 0$ in lattice unit (refer to Fig. 2). Here V has unit of lu³.

In the implementation, we take the following form [26],

$$\frac{\partial \phi}{\partial \tau_3} + \mathbf{u} \cdot \nabla \phi = 0, \tag{28}$$

where $\mathbf{u} = (u_x, u_r) = -(V - V_0) \nabla \phi / |\nabla \phi|$. Although a high-order scheme can be used to solve this equation [26], here for simplicity the first-order upwind finite difference scheme is used to discretize the convection term, i.e., $\mathbf{u} \cdot \nabla \phi$. The first-order Euler's scheme is used to discretize the time derivative.

For example, if $u_x > 0$, $\partial_x^- \phi = \frac{\phi_{(i,j)} - \phi_{(i-1,j)}}{\delta x}$, if $u_x < 0$, $\partial_x^+ \phi = \frac{\phi_{(i+1,j)} - \phi_{(i,j)}}{\delta x}$. In our simulations solving this equation, the time step $d\tau_3 \sim \frac{0.15}{V_0}$ is adopted. If $u_x^+ = \max(u_x, 0)$ and $u_x^- = \min(u_x, 0)$ are defined in the x -axis, and the corresponding variables in r direction are defined similarly, then the discretize form can be written as

$$\phi_{(i,j)}^{\tau+d\tau_3} = \phi_{(i,j)}^\tau - (u_x^+ \partial_x^- \phi + u_x^- \partial_x^+ \phi) d\tau_3 - (u_r^+ \partial_r^- \phi + u_r^- \partial_r^+ \phi) d\tau_3. \tag{29}$$

2.5. Axisymmetric boundary condition

In our simulation, one boundary ($r = 0$) represents the axisymmetric axis and the other three boundaries ($x = 0$, $x = L$, and $r = \frac{D^r}{2}$) are walls. For the walls, the non-slip wall boundary condition is imposed. In the LBM, corresponding simple bounce-back scheme is used to get the unknown f_i , g_i in the inward direction after the streaming step. In the scheme, these unknown distribution functions are set to be the distribution functions in the corresponding reverse directions. For example, after the streaming step, f_4 , f_7 , and f_8 are unknown in the upper wall boundary (refer to Fig. 2); they are set to be $f_4 = f_2$, $f_7 = f_5$, and $f_8 = f_6$.

The source terms and boundary condition in the axisymmetric axis should be paid more attention. For the source terms like $\rho \frac{u_r}{r}$, we should handle it carefully. According to l'Hôpital's rule law, we have $\lim_{r \rightarrow 0} \rho \frac{u_r}{r} = \rho \partial_r u_r$. Hence, after we got $\partial_r u_r$ using the finite difference scheme, $\lim_{r \rightarrow 0} \rho \frac{u_r}{r}$ is obtained. For both f_i and g_i in the x -axis, the slip boundary condition should be applied. For example, in the x -axis (refer to Fig. 2), the unknown distribution functions are f_2 , f_5 , and f_6 . These unknowns after streaming step can be obtained through setting $f_2 = f_4$, $f_5 = f_8$, and $f_6 = f_7$.

Table 1

Cases for bubble rising ($\sigma = 0.011\kappa$, $\nu_l = (\tau_l - 0.5)c_s^2\delta t$, $D = 100$ lu, tube diameter $D_T = 5D$ and density ratio 15.5).

Case	Eo	Mo	Re. [22]	τ_l	κ	g	Re. (LBM)
A1	17.7	711	0.232	0.862	0.0005	4.06×10^{-8}	0.288
A2	32.2	8.2×10^{-4}	55.3	0.54081	0.008	1.18×10^{-6}	48.4
A3	243	266	7.77	0.9155	0.004	4.46×10^{-6}	6.93
A4	115	4.63×10^{-3}	94	0.536	0.005	2.64×10^{-6}	83.7
A5	339	43.1	18.3	0.710	0.003	4.66×10^{-6}	17.0
A6	641	43.1	30.3	0.646	0.002	5.88×10^{-6}	27.7
A7	116	5.51	13.3	0.712	0.005	2.66×10^{-6}	12.0
A8	114	8.6×10^{-4}	151	0.5238	0.005	2.61×10^{-6}	131.3
A9	116	0.103	42.2	0.578	0.005	2.66×10^{-6}	36.0
B1	94.3	4.85×10^{-3}	77.9	0.5487	0.008	3.46×10^{-6}	70.2
B2	61.9	8.2×10^{-4}	99.5	0.5274	0.005	1.42×10^{-6}	82.6
B3	292	26.7	22.1	0.750	0.005	6.69×10^{-6}	16.6

3. Numerical validation

In this section, all typical terminal bubble shapes are observed in our simulations. The mass conservation property of our model, the effect of different surface tension calculations, the density ratio effects on the terminal shape and velocity are investigated in the following subsections. The terminal bubble shapes and velocities are compared with the experimental data in detail. Finally we demonstrate that our axisymmetric model is able to reproduce the effect of initial bubble shape in Ref. [30].

In the literature, usually two independent non-dimensional numbers: Eötvös number and Morton number for bubble rising problems are defined [22]:

$$Eo = \frac{gD^2\rho_l}{\sigma}, \tag{30}$$

$$Mo = \frac{g\mu_l^4}{\rho_l\sigma^3}. \tag{31}$$

The Reynolds number is based on terminal bubble rising velocity U_t and initial bubble diameter D , i.e., $Re = \frac{U_t D}{\nu_l}$, where ν_l is the kinematic viscosity of liquid.

Table 1 illustrates the main parameters used in our simulations. In these simulations, the typical terminal bubble shapes, such as spherical, oblate ellipsoidal, disk, spherical cap, and skirted are all observed. To compare with the experimental setting, the tube diameter in our simulation is $D_T = 5D$. All of the initial bubbles are supposed to be spherical except simulations in Section 3.7. From the regime map of the experimental observation, we know that at high Reynolds number and high Eo number, the bubble may rise in a wobbly path, which is not axisymmetric flow. Here the bubble rising under this extreme conditions is not considered.

In the LBM simulations, to ensure better incompressibility conditions, the maximum velocity magnitude should not exceed 0.1 lu/ts. In Table 1, all terminal Res are known from experiment [22], so we can calculate the expected terminal velocity in the LBM simulations. From the calculation, the expected rising velocities are all less than 0.02 lu/ts, which sufficiently satisfies the incompressible condition well. For this unsteady flow problem, a smaller time step is preferred. Hence, smaller τ is preferred in the simulations. On the other hand, smaller τ may induce numerical instability. The parameters are chosen according to a balance between the two constraints.

In the simulations, it is found that the maximum density ratio $\frac{\rho_l}{\rho_g}$ can be slightly larger than $\frac{\phi_l}{\phi_g}$. In all of the simulations in Table 1, we set $\rho_l = 0.247$ mu/lu³, and $\rho_g = 0.016$ mu/lu³, which means the maximum density ratio in our simulations is $\frac{\rho_l}{\rho_g} = 15.5$. In Section 3.4, the effect of density ratio will be discussed.

In Table 1, first we can set $\kappa \approx O(0.001)$, then the surface tension is calculated through $\sigma = 0.011\kappa$ (the relationship is measured from the Laplace law). The acceleration of gravity is determined from $g = \frac{\sigma Eo}{D^2\rho_l}$. The kinematic viscosity of the liquid is determined through

$$\nu_l = \left(\frac{D^2\sigma^2 Mo}{\rho_l^2 Eo} \right)^{\frac{1}{4}}. \tag{32}$$

The relaxation time for liquid is $\tau_l = \frac{\nu_l}{c_s^2\delta t} + 0.5$.

Although the relaxation time for gas τ_g is not necessary to be identical to τ_l , here $\tau_2 = \tau_g = \tau_l$ is adopted in simulations in Table 1. We will demonstrate this assumption is acceptable in the following Section 3.1.

Our LBM result about terminal bubble rising Res are listed in the rightmost column of the table, and compared to the Res measured from experiments [22]. In Section 3.4, the comparison will be discussed in detail.

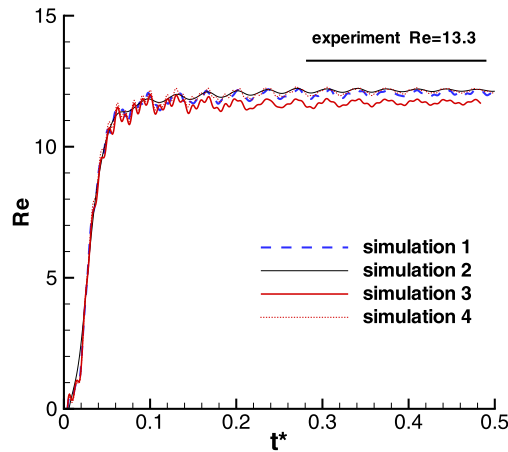


Fig. 3. Four simulations for case A7 (refer to Table 1, $\tau_l = 0.712$). In simulations 1, 2, and 3, the kinematic viscosities of gas are $\nu_g = \nu_l$, $\nu_g = \frac{1}{2}\nu_l$, $\nu_g = 4\nu_l$, respectively. In these three simulations $\tau_2 = \tau_l$. In simulation 4, $\nu_g = \nu_l$ and $\tau_2 = 1.0$.

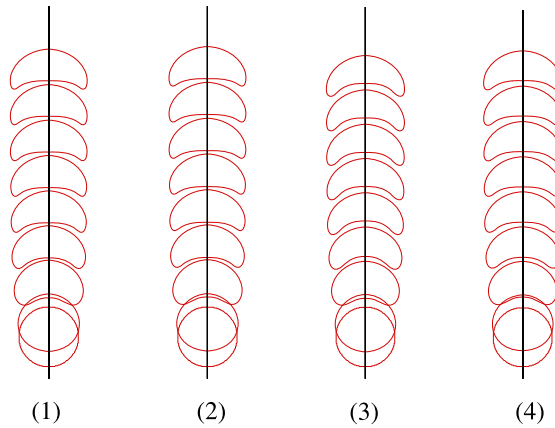


Fig. 4. Bubble evolution in the four simulations for case A7 (refer to Table 1), the time interval of each snapshot is $t^* = 0.0494$. Parameters of simulations 1 to 4 are shown in the caption of Fig. 3.

3.1. τ -Effect

To demonstrate τ -effect on bubble rising, we take case A7 as an example (density ratio is fixed to be 15.5). Four simulations with different kinematic viscosity ratio $\frac{\nu_l}{\nu_g}$ are performed. The rising velocities for the four simulations (case A7) as a function of time are shown in Fig. 3. Fig. 4 shows the bubble evolution in the four simulations. The time is normalized by $t^* = t \frac{\nu_l}{D^2}$, where t is the time steps in simulations. In the simulations 1, 2, and 3, $\tau_2 = \tau_l$ is adopted while τ_g is different. From Fig. 3, it is seen that although τ_g 's are different, rising velocities in simulation 2 ($\nu_g = \frac{1}{2}\nu_l$) and simulation 3 ($\nu_g = 4\nu_l$) are almost identical to that of simulation 1. Hence, the simulation result is not sensitive to the kinematic viscosity ratio in the range of $\frac{1}{4} < \frac{\nu_l}{\nu_g} < 2$.

As we know when the mobility changes in a proper range, the mobility does not affect the simulation results [31]. Since the mobility is related to τ_2 , here τ_2 -effect is studied. From the comparison of simulations 1 and 4 in Fig. 3 and Fig. 4, it is seen that no matter if $\tau_2 = 1$ or $\tau_2 = \tau_l$, parameter τ_2 almost does not affect the numerical result in terms of rising velocity and bubble evolution. Although τ_2 and τ_g is adjustable, the maximum density ratio in our simulation is not improved through changing τ_2 or τ_g .

In the following Section 3.4, we will see that the density ratio has more significant effect on the bubble rising behavior than the kinematic viscosity ratio. In all of the following simulations, $\tau_2 = \tau_g = \tau_l$ is adopted for simplicity.

3.2. Mass conservation

The mass correction issue is one of the key issues we pay special attention to. Case A2 is simulated with and without mass correction step. The result of the mass ratio $\frac{V(t)}{V_0}$ is shown in Fig. 5, where $V(t)$ is the bubble volume at time t . It is

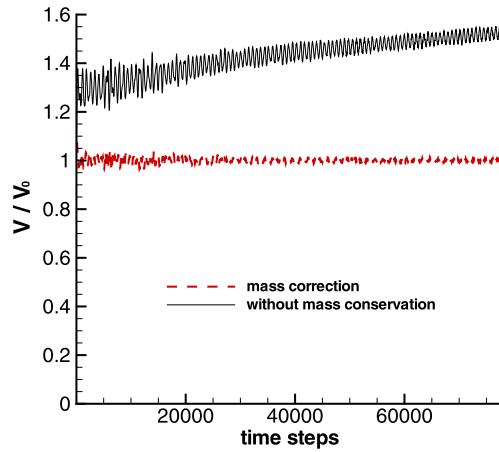


Fig. 5. Thick dashed line and the thin solid line represent the mass ratio $\frac{V}{V_0}$ as a function of time with and without mass correction, respectively. Case A2 in Table 1 is simulated.

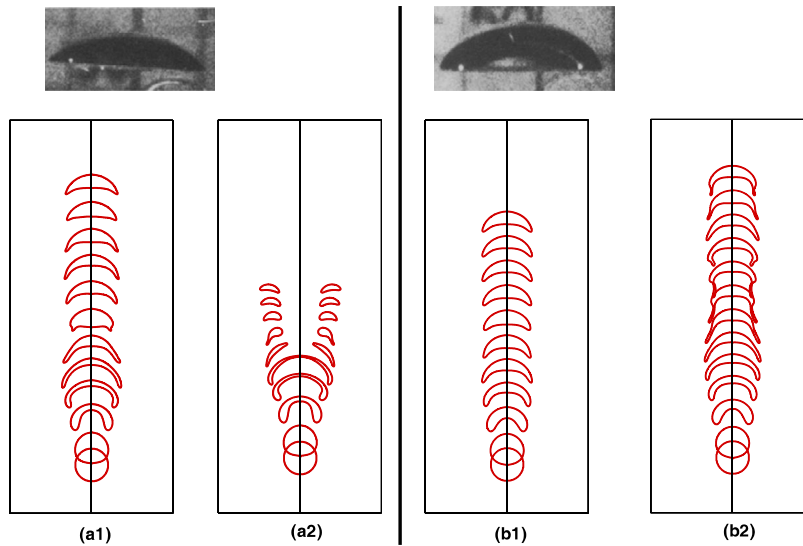


Fig. 6. Surface-tension-calculation effect on bubble shape evolution. Topleft and topright photographs are the experiment results [22] for cases A4 and A9, respectively. (a1) Bubble shape evolution of case A4 with revised surface tension calculation; (a2) case A4 with original surface tension calculation; (b1) case A9 with revised surface tension calculation; (b2) case A9 with original surface tension calculation. Parameters in cases A4 and A9 are illustrated in Table 1. The horizontal is r -direction.

seen that without the mass correction step, $\frac{V}{V_0}$ increases rapidly at the initial stage and then increases slowly with time. In other words, the bubble continuously grows up.

For the simulation with mass correction (the dashed line in Fig. 5), the bubble volume is almost kept constant although there is very small oscillation. The small oscillation may be due to the simple upwind scheme we used. If essentially non-oscillatory (ENO) scheme [26] is used, the oscillation may be eliminated. However, due to simplicity, the simple upwind scheme and the first-order Euler's scheme are still recommended.

3.3. Surface-tension-calculation effect

After revising the type of Premnath [23], it is expected that the axisymmetric model is able to simulate the bubble rising correctly. However, in this section we can see that without the revised surface tension calculation mentioned in Section 2.3, the axisymmetric HCZ model [24] can only give poor result compared to the experimental result.

Cases A4 and A9 were simulated to compare the effect of surface-tension-calculation schemes. Results about bubble shapes evolution as they rise are shown in Fig. 6. In the figure, columns (a1) and (a2) represent the results of case A4 with revised and original surface tension calculations, respectively. The time interval of each snapshot is $t^* = 0.012$. It is seen that with the original surface tension calculation, the bubble becomes toroidal (refer to (a2)), which is very different

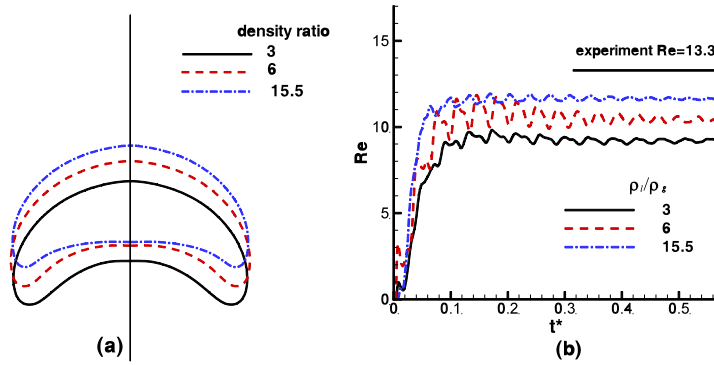


Fig. 7. Density ratio effects on (a) shape and (b) rising velocity of bubble (Case A7).

from the experimental photograph shown in the topleft of Fig. 6. On the contrary, the result with revised surface tension calculation (refer to (a1)) is very consistent with the experiment data.

For case A9, from Fig. 6 (b1) and (b2), we can see that with the revised surface tension calculation, the terminal bubble shape in (b1) is very consistent with the result of experiment [22]. The time interval of each snapshot is $t^* = 0.026$. The bubble shapes in (b2) still have some discrepancies with the experimental photograph. It is noticed that in the above simulations, the mass conservation is ensured through the mass correction step.

3.4. Density ratio effect

Here in our simulations, the density ratio is not able to reach 1000, which is the density ratio in many bubble rising experiments [22]. Hua and Lou [30] found that effect of density ratio is more significant in terminal velocity than in terminal shape. In this section, the effects of density ratio (or dynamic viscosity ratio) on the terminal velocity and bubble shape are investigated. Here case A7 is extensively simulated under different density ratio. In the simulations, the kinematic viscosities for the fluid and gas are identical, which means $\tau_1 = \tau_g = \tau_l$.

The terminal bubble shapes for different density ratio are shown in Fig. 7(a). The rising velocities as a function of time are illustrated in Fig. 7(b). It is seen that the bubble shapes are not affected much by density ratios. From Fig. 7(b), we can see that the rising velocities all increase rapidly at first and reach their equilibrium terminal values with small amplitude oscillations. The Re in the experiment is 13.3. For density ratios 3, 6, 15.5, the terminal Re s are 9.3, 10.9, and 12.0, respectively. Hence, with density ratio $O(10)$, the terminal simulated Re seems very close to the experimental one. From Fig. 7(a) and (b), we also found that the effect of density ratio is more significant in terminal velocity than in terminal shape. These conclusions are consistent with those of Hua and Lou [30].

The maximum density ratio in our simulations is about 15.5. From the above discussion we know that using this density ratio, we can get the terminal rising velocity very close to the experimental data (density ratio 1000). The simulated terminal Re s for the other cases are also compared with the experimental ones in Table 1. The measured Re s from LBM simulation on the rightmost column of the table agree well with the experimental Re s from Ref. [22].

For the cases with very small Mo (high Re), such as A2, A4, A8, B1 and B2 in Table 1, numerical instability may appear if the BGK collision model is used and τ_1, τ_2 are small. For these cases, the simulations with density ratio $\frac{\rho_l}{\rho_g} = 15.5$ are not applicable using the BGK collision model. Hence, the MRT collision is used for these simulations with $\frac{\rho_l}{\rho_g} = 15.5$. The rising Re from our MRT LBM simulation are illustrated in Table 1, which have small discrepancies (about 10%) with the experiment data because the density ratio is not so high as that in the experiment [22].

3.5. Terminal bubble shape

In principle, the surface tension force tends to maintain the bubble to be spherical. For cases with specific density, bubble diameter, and acceleration of gravity, a high Eo number means low surface tension, which allows large deformation [30]. On the other hand, higher Re would induce larger deformation in the bubble's vertical direction [30]. The final bubble shape is determined by the combination effect of Eo and Re . Fig. 8 shows the terminal bubble shapes comparison with the experimental data [22] in six cases. For case A1, due to small Eo and Re (refer to Table 1), the bubble remains almost spherical when it rises. The final bubble shape in case A2 is oblate ellipsoidal (disk like). In case A3 the bubble shape is an oblate ellipsoidal cap. At lower part of the bubble, there is a rounded lower edge. Due to high Re , the bubble shape in case A4 is a spherical cap. Due to large Eo , both terminal bubble shapes in cases A5 and A6 are skirted. The shapes all agree well with both the experimental ones [22] and the numerical ones using finite volume scheme [30].

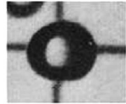








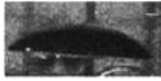




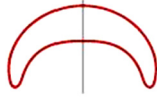



case	experiments	Hua, JCP 2007	LBM
A1	$E=17.7$ $M=711$ 		
A2	$E=32.2$ $M=8.2 \times 10^{-4}$ 		
A3	$E=243$ $M=266$ 		
A4	$E=115$ $M=4.63 \times 10^{-3}$ 		
A5	$E=339$ $M=43.1$ 		
A6	$E=641$ $M=43.1$ 		

Fig. 8. Comparison of terminal bubble shapes observed in experiments and predicted in LBM (A1–A6) of various Eo and Mo . Left, middle, and right columns represent experiment results [22], results from Hua and Lou [30], and LBM results, respectively.

3.6. Wake behind the bubble

To further validate our LBM scheme, the wake behind the bubble is compared with the observation in the experiment [22]. In the experiment, H_2 tracer was used to obtain the flow visualization. Fig. 9 shows the terminal bubble wakes in three cases B1, B2, and B3. The main parameters used in the simulations are illustrated in Table 1. In each case, the closed toroidal wake predicted by our LBM simulation agrees well with the experimental one. For case B1, which is shown in Fig. 9(a), there are some bright spots at the lower outside of bubble rim in the experiment photograph. The possible reason is that secondary wake circulations occur just behind the bubble rim. Indeed in our LBM simulation, there are two small secondary wakes. In case B2 (Fig. 9(b)), the secondary wake is not observed. In case B3 (Fig. 9(c)), the secondary circulation area in the skirt bubble wake becomes larger. The LBM results are very consistent with both the numerical [30] and experimental [22] studies.

3.7. Effect of initial bubble shape

Hua and Lou [30] discussed the effect of initial bubble shape on the bubble rising. They found that for bubble rising with the lower Reynolds number, the terminal bubble shape and rising velocity are almost not affected by the initial bubble shape. However, for the high- Re cases, the initial bubble shapes would significantly affect the terminal bubble shapes [30]. In this section, we can see that our LBM successfully reproduces the effect of initial bubble shape in Ref. [30].

Fig. 10 shows the evolution of the bubble shape under conditions of two different initial bubble shapes for case A8. Through comparison between (a) and (b), we can see the final bubble shape depends on the initial bubble shape. When the bubble aspect ratio is initially small (refer to Fig. 10(a)), the bubble may rise slowly due to relatively large drag force on the bubble. Hence only a weak liquid jet would form at the bubble bottom [30]. Finally, the bubble becomes a spherical cap. For the case with an initial spherical bubble (refer to Fig. 10(b)), the toroidal bubble is predicted. These phenomena have been observed in numerical simulations [30]. The present axisymmetric LBM is able to reproduce the effect of initial bubble shape [30].

On the other hand, for this case (case A8), the spherical cap bubble was observed in the experiment [22]. Why in the experiment the terminal bubble is a spherical cap can be understood as following. In the experiments, the initial bubble shapes are usually assumed to be spherical. However, this may not be true. It is noticed that in the experiment [22], the bubble was first hold by a hemi-spherical dumping cup with a relatively large size, and then released. When it was hold, a large bubble may deform to ellipsoidal shape due to the smaller surface tension force and stronger buoyancy force [30].

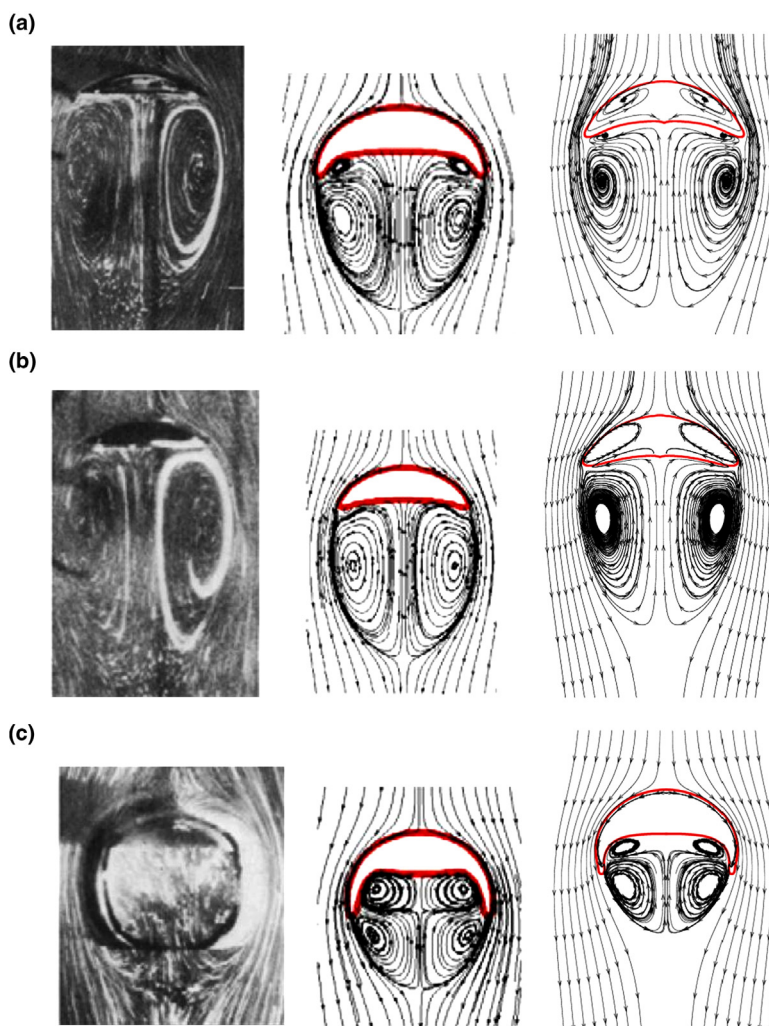


Fig. 9. Terminal bubble wakes in (a) case B1 (upper row); (b) case B2 (middle row); (c) case B3 (bottom row). The left, middle, and right columns are results from experiment [22], numerical work [30], and our LBM, respectively.

Hence, our predicted bubble shape agree well with the experimental one as long as the initial bubble shape is oblate in the experiment [22].

4. Conclusions

We developed a mass-conserving axisymmetric HCZ model. Due to the revised surface tension calculation, bubble rising shape is consistent with experimental result and the effect of initial bubble shape were reproduced successfully. In our simulations, the terminal bubble rising velocities are very consistent with the experimental ones. Quantitatively, the wakes behind the bubble agree well with the experimental ones and those of Hua and Lou [30].

Through adopting the mass correction step in our scheme and using a revised surface tension calculation, present axisymmetric multiphase LB model is more superior than the previous one [23] for bubble rising problem.

For high-density-ratio issue, developing a Lee–Lin model [2] based axisymmetric LBM [23] may be able to handle the high-density-ratio bubble rising flows. However, 3D simulations using Lee–Lin model about bubble rising is not so satisfactory [4], whether good numerical results can be achieved in axisymmetric simulations (based on the Lee–Lin model) is an open question. High-density-ratio is an important issue we will work on in the near future.

Acknowledgements

This work was supported by the National Science Foundation of China (NSFC) (Grant No. 10802085). It is also supported by Program for New Century Excellent Talents in University (NCET-12-0506), Ministry of Education, China.

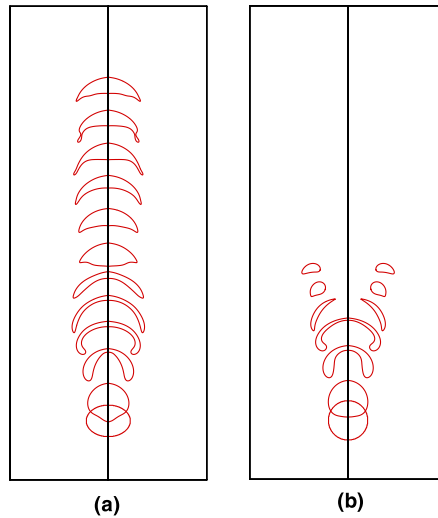


Fig. 10. The evolution of the bubble shape at time interval $t^* = 7.93e-3$ for case A8. (a) Initially an oblate bubble, aspect ratio between height and width of the initial bubble is 0.716; (b) initially a spherical bubble.

Appendix A. Chapman–Enskog analysis

Applying Taylor expansion on Eq. (9), and adopt Chapman–Enskog expansion $\partial_t = \partial_{t_1} + \epsilon \partial_{t_2} + \dots$ and $\bar{g}_i = \bar{g}_i^{(0)} + \epsilon \bar{g}_i^{(1)} + \epsilon^2 \bar{g}_i^{(2)}$, where $\epsilon = \delta t$, we have

$$\begin{aligned} &\epsilon(\partial_{t_1} + \epsilon \partial_{t_2} + e_{i\alpha} \partial_\alpha)(\bar{g}_i^{(0)} + \epsilon \bar{g}_i^{(1)} + \epsilon^2 \bar{g}_i^{(2)}) \\ &+ \frac{\epsilon^2}{2}(\partial_{t_1} + \epsilon \partial_{t_2} + e_{i\alpha} \partial_\alpha)^2(\bar{g}_i^{(0)} + \epsilon \bar{g}_i^{(1)}) \\ &= -\frac{1}{\tau_1}(\bar{g}_i^{(0)} + \epsilon \bar{g}_i^{(1)} + \epsilon^2 \bar{g}_i^{(2)} - \bar{g}_i^{(eq)}) + S_i \delta t \end{aligned} \tag{33}$$

Retaining terms to $O(\epsilon^2)$, in different time scale, Eq. (33) yield

$$O(\epsilon): (\bar{g}_i^{(0)} - \bar{g}_i^{eq})/\tau_1 = 0, \tag{34}$$

$$O(\epsilon^1): (\partial_{t_1} + e_{i\alpha} \partial_\alpha) \bar{g}_i^{(0)} + \frac{1}{\tau_1} \bar{g}_i^{(1)} - S_i = 0, \tag{35}$$

$$O(\epsilon^2): \partial_{t_2} \bar{g}_i^{(0)} + \left(1 - \frac{1}{2\tau_1}\right)(\partial_{t_1} + e_{i\alpha} \partial_\alpha) \bar{g}_i^{(1)} + \frac{1}{2}(\partial_{t_1} + e_{i\alpha} \partial_\alpha) S_i + \frac{1}{\tau_1} \bar{g}_i^{(2)} = 0. \tag{36}$$

A.1. Preparation

We note that Eq. (14) yields $\sum \bar{g}_i = \sum \bar{g}_i^{(0)} + \delta t \sum \bar{g}_i^{(1)} + \delta t^2 \sum \bar{g}_i^{(2)} + \dots = (p_h - \frac{\delta t}{2} u_\beta E_\beta) + c_s^2 \frac{\rho u_r}{2r} \delta t$. From Eq. (34) and Eq. (12), we have

$$\sum \bar{g}_i^{(0)} = \sum \bar{g}_i^{eq} = p_h. \tag{37}$$

Hence, from the above two equations, we can derive

$$\sum \bar{g}_i^{(1)} = -\frac{1}{2} u_\beta E_\beta + c_s^2 \frac{\rho u_r}{2r}, \quad \sum \bar{g}_i^{(2)} = 0. \tag{38}$$

Similarly, from Eq. (15), we can obtain $\sum e_{i\alpha} \bar{g}_i = \sum e_{i\alpha} \bar{g}_i^{(0)} + \delta t \sum e_{i\alpha} \bar{g}_i^{(1)} = c_s^2 (\rho u_\alpha - \frac{\delta t}{2} F_\alpha)$. Hence, the first moments of $\bar{g}_i^{(0)}$ and $\bar{g}_i^{(1)}$ are

$$\sum e_{i\alpha} \bar{g}_i^{(0)} = c_s^2 \rho u_\alpha, \quad \sum e_{i\alpha} \bar{g}_i^{(1)} = -\frac{1}{2} F_\alpha c_s^2. \tag{39}$$

The zeroth and first moments of the source term S_i take the form

$$\sum_i S_i = \left(1 - \frac{1}{2\tau_1}\right) \left\{ u_\alpha E_\alpha - c_s^2 \frac{\rho u_r}{r} \right\}, \quad \sum_i e_{i\beta} S_i = c_s^2 \left(1 - \frac{1}{2\tau_1}\right) F_\beta. \tag{40}$$

To be well-prepared for the further derivation, we also write down the second moment of $\bar{g}_i^{(0)}$ and S_i . From Eq. (37), we have

$$\sum g_i^{(0)} e_{i\alpha} e_{i\beta} = c_s^2 (p_h \delta_{\alpha\beta} + \rho u_\alpha u_\beta). \tag{41}$$

Using Eq. (18) and omitting higher order terms of $O(u^3)$, we have

$$\sum e_{i\alpha} e_{i\beta} S_i = c_s^2 \left(1 - \frac{1}{2\tau_1}\right) \left\{ E_\gamma (u_\alpha \delta_{\beta\gamma} + u_\beta \delta_{\alpha\gamma} + u_\gamma \delta_{\beta\alpha}) + (F_\beta u_\alpha + F_\alpha u_\beta) - c_s^2 \frac{\rho u_r}{r} \delta_{\alpha\beta} \right\}. \tag{42}$$

A.2. Mass conservation

Summing both sides of Eq. (35) over i and using Eqs. (37), (38), and (40) gives

$$\partial_{t_1} p_h + c_s^2 \partial_\alpha (\rho u_\alpha) - u_\alpha E_\alpha + c_s^2 \frac{\rho u_r}{r} = (\partial_{t_1} + u_\alpha \partial_\alpha) p_h + c_s^2 \left(\rho \partial_\alpha u_\alpha + \frac{\rho u_r}{r} \right) = 0. \tag{43}$$

Then we proceed to $O(\epsilon^2)$. Using Eqs. (37), (38), (39), and (40) and summing both sides of Eq. (36) over i gives

$$\partial_{t_2} p_h = 0. \tag{44}$$

From Eqs. (43) and (44), we obtained

$$(\partial_t + u_\alpha \partial_\alpha) p_h + c_s^2 \left(\rho \partial_\alpha u_\alpha + \frac{\rho u_r}{r} \right) = 0. \tag{45}$$

Here we can see that only when $(\partial_t + u_\alpha \partial_\alpha) p_h = 0$, the incompressible condition $\rho \partial_\alpha u_\alpha + \frac{\rho u_r}{r} = 0$ can be satisfied.

A.3. Momentum conservation

Multiplying Eq. (35) by $e_{i\beta}$ and summing over i and using Eqs. (40) and (41) gives

$$O(\epsilon): \quad \partial_{t_1} (\rho u_\beta) + \partial_\alpha (p_h \delta_{\alpha\beta} + \rho u_\alpha u_\beta) - F_\beta = 0. \tag{46}$$

Multiplying Eq. (36) by $e_{i\beta}$ and summing over i gives

$$O(\epsilon^2): \quad c_s^2 \partial_{t_2} (\rho u_\beta) + \left(1 - \frac{1}{2\tau_1}\right) \left[\partial_{t_1} \left(\sum e_{i\beta} \bar{g}_i^{(1)} \right) + \partial_\alpha \left(\sum e_{i\alpha} e_{i\beta} \bar{g}_i^{(1)} \right) \right] + \frac{1}{2} \left[\partial_{t_1} \left(\sum e_{i\beta} S_i \right) + \partial_\alpha \sum (e_{i\beta} e_{i\alpha} S_i) \right] = 0. \tag{47}$$

From Eqs. (39) and (40), we know that

$$\left(1 - \frac{1}{2\tau_1}\right) \partial_{t_1} \left(\sum e_{i\beta} \bar{g}_i^{(1)} \right) = c_s^2 \left(1 - \frac{1}{2\tau_1}\right) \partial_{t_1} \left(-\frac{1}{2} F_\alpha \right) = -\frac{1}{2} \partial_{t_1} \left(\sum e_{i\beta} S_i \right). \tag{48}$$

Hence, Eq. (47) can be simplified as

$$c_s^2 \partial_{t_2} (\rho u_\beta) + \left(1 - \frac{1}{2\tau_1}\right) \partial_\alpha \sum (e_{i\alpha} e_{i\beta} \bar{g}_i^{(1)}) + \frac{1}{2} \partial_\alpha \sum (e_{i\beta} e_{i\alpha} S_i) = 0. \tag{49}$$

To perform derivation, our temporal task now is to get $\sum (e_{i\alpha} e_{i\beta} \bar{g}_i^{(1)})$. We note from Eq. (35) that $\bar{g}_i^{(1)} = -\tau_1 (\partial_{t_1} + e_{i\alpha} \partial_\alpha) \bar{g}_i^{(0)} + \tau_1 S_i$. Substituting this equation into Eq. (49), Eq. (49) is further simplified as

$$c_s^2 \partial_{t_2} (\rho u_\beta) - (\tau_1 - 0.5) \partial_\alpha \sum (e_{i\alpha} e_{i\beta} (\partial_{t_1} + e_{i\gamma} \partial_\gamma) \bar{g}_i^{(0)}) + \tau_1 \partial_\alpha \sum (e_{i\beta} e_{i\alpha} S_i) = 0. \tag{50}$$

Eq. (50) includes the third moments of $\bar{g}_i^{(0)}$. From Eq. (12), we have

$$\partial_\gamma \sum (e_{i\alpha} e_{i\beta} e_{i\gamma} \bar{g}_i^{(0)}) = c_s^4 \partial_\gamma [\rho (u_\alpha \delta_{\beta\gamma} + u_\beta \delta_{\alpha\gamma} + u_\gamma \delta_{\beta\alpha})]. \tag{51}$$

Substituting Eqs. (41), (42) and (51) into Eq. (50) gives

$$\begin{aligned} & \partial_{t_2}(\rho u_\beta) - (\tau_1 - 0.5) \left\{ \partial_\alpha \partial_{t_1} (p_h \delta_{\alpha\beta}) + \underbrace{\partial_\alpha \partial_{t_1} (\rho u_\alpha u_\beta)} + c_s^2 \partial_\alpha \partial_\gamma [\rho (u_\alpha \delta_{\beta\gamma} + u_\beta \delta_{\alpha\gamma} + u_\gamma \delta_{\beta\alpha})] \right\} \\ & + (\tau_1 - 0.5) \left\{ \underbrace{\partial_\alpha [F_\beta u_\alpha + F_\alpha u_\beta]} + \partial_\alpha \left[E_\gamma (u_\alpha \delta_{\beta\gamma} + u_\beta \delta_{\alpha\gamma} + u_\gamma \delta_{\beta\alpha}) - c_s^2 \frac{\rho u_r \delta_{\alpha\beta}}{r} \right] \right\} \\ & = 0. \end{aligned} \tag{52}$$

In Appendix B, we will show that the underbraced terms in Eq. (52) can be canceled. From Eq. (43), we know

$$\partial_{t_1} (p_h \delta_{\alpha\beta}) = \left\{ -c_s^2 \left[\partial_\gamma (\rho u_\gamma) + \frac{\rho u_r}{r} \right] + u_\gamma E_\gamma \right\} \delta_{\alpha\beta}. \tag{53}$$

Substituting this equation and $E_\gamma = -\partial_\gamma (p_h - c_s^2 \rho)$ into Eq. (52), and noticing the terms $u_\alpha \partial_\beta p_h$, $u_\beta \partial_\alpha p_h$ will be canceled with their counterparts in $\partial_{t_1} (\rho u_\alpha u_\beta)$ (see Appendix B), it yields

$$\partial_{t_2}(\rho u_\beta) - c_s^2 (\tau_1 - 0.5) \partial_\alpha \{ \rho [\partial_\beta u_\alpha + \partial_\alpha u_\beta] \} = 0. \tag{54}$$

From Eqs. (46) and (54), using $\partial_t(\rho u_\beta) = \partial_{t_1}(\rho u_\beta) + \delta t \partial_{t_2}(\rho u_\beta)$ and $\nu = c_s^2 (\tau_1 - 0.5) \delta t$, we have the Navier–Stokes equations,

$$\partial_t(\rho u_\beta) + \partial_\alpha(\rho u_\alpha u_\beta) = -\partial_\beta p_h + \nu \partial_\alpha \{ \rho [\partial_\beta u_\alpha + \partial_\alpha u_\beta] \} + F_\beta. \tag{55}$$

A.4. Cahn–Hilliard equation

To obtain the equation tracking interface, we start from the equation analogous to Eqs. (34)–(36) for the distribution functions \tilde{f}_i . From Eq. (16) and Eq. (33), we know that $\sum_i \tilde{f}_i^{(0)} = \phi$, $\sum_i \tilde{f}_i^{(1)} = \frac{\phi u_r}{2r}$, and $\sum_i \tilde{f}_i^{(n)} = 0$, for $n > 1$. Summing both sides of Eq. (35) over i yields

$$\partial_{t_1} \phi + \partial_\alpha (\phi u_\alpha) + \frac{\phi u_r}{r} = 0. \tag{56}$$

Summing Eq. (36) over i and substituting $\sum S'_i = -(1 - \frac{1}{2\tau_2}) \frac{\phi u_r}{r}$ yields

$$\partial_{t_2} \phi + \left(1 - \frac{1}{2\tau_2} \right) \left[\partial_\alpha \left(\sum_i e_{i\alpha} \tilde{f}_i^{(1)} \right) + \partial_{t_1} \left(\frac{\phi u_r}{2r} \right) \right] + \frac{1}{2} \left[\partial_\alpha \left(\sum_i e_{i\alpha} S'_i \right) - \left(1 - \frac{1}{2\tau_2} \right) \partial_{t_1} \left(\frac{\phi u_r}{r} \right) \right] = 0. \tag{57}$$

In the simulation $\sum \tilde{f}_i e_{i\alpha}$ is unknown or not calculated. Hence, although $\sum \tilde{f}_i^{eq} e_{i\alpha}$ is known, it is impossible to determine $\sum_i e_{i\alpha} \tilde{f}_i^{(1)}$ in the LBM. If this term is assumed to be omitted, substituting $\sum_i e_{i\alpha} S'_i = (1 - \frac{1}{2\tau_2}) F'_\alpha$, Eq. (57) yields

$$\partial_{t_2} \phi + \frac{1}{2} \left(1 - \frac{1}{2\tau_2} \right) \partial_\alpha F'_\alpha = 0. \tag{58}$$

Substituting $F'_\alpha = -\partial_\alpha (p_{th} - c_s^2 \phi)$ into above equation, we have

$$\partial_{t_2} \phi = \frac{1}{2} \left(1 - \frac{1}{2\tau_2} \right) \partial_\alpha (\partial_\alpha (p_{th} - c_s^2 \phi)). \tag{59}$$

Combining Eqs. (56) and (59) together gives

$$\partial_t \phi + \partial_\alpha (\phi u_\alpha) + \frac{\phi u_r}{r} = \lambda \partial_\alpha^2 (p_{th} - c_s^2 \phi), \tag{60}$$

where $\lambda = \frac{1}{2} (1 - \frac{1}{2\tau_2}) \delta t$. This is the macro phase-tracking equation, which is a Cahn–Hilliard-like equation in our axisymmetric model based on HCZ model [1].

Appendix B

Here to prove the term $\partial_{t_1} (\rho u_\alpha u_\beta)$ in Eq. (52) and the term $\partial_\alpha [F_\beta u_\alpha + F_\alpha u_\beta]$ in Eq. (42) can be canceled. From Eq. (46), we know that

$$u_\alpha \partial_{t_1} (\rho u_\beta) = -u_\alpha \partial_\alpha (p_h \delta_{\alpha\beta} + \rho u_\alpha u_\beta) + u_\alpha F_\beta, \tag{61}$$

and

$$u_\beta \partial_{t_1} (\rho u_\alpha) = -u_\beta \partial_\beta (p_h \delta_{\alpha\beta} + \rho u_\alpha u_\beta) + u_\beta F_\alpha. \tag{62}$$

Substituting the above two equations into $\partial_{t_1}(\rho u_\alpha u_\beta) = u_\alpha \partial_{t_1}(\rho u_\beta) + u_\beta \partial_{t_1}(\rho u_\alpha) - u_\alpha u_\beta \partial_{t_1} \rho$, we have

$$\begin{aligned} \partial_{t_1}(\rho u_\alpha u_\beta) &= -u_\alpha \partial_\alpha (p_h \delta_{\alpha\beta} + \rho u_\alpha u_\beta) - u_\beta \partial_\beta (p_h \delta_{\alpha\beta} + \rho u_\alpha u_\beta) \\ &\quad + (u_\beta F_\alpha + u_\alpha F_\beta) - u_\alpha u_\beta \partial_{t_1} \rho. \end{aligned} \quad (63)$$

We note that in the above equation, the terms $u_\alpha \partial_\beta p_h$, $u_\beta \partial_\alpha p_h$ will be canceled with their counterparts in Eq. (52). Terms $u_\alpha \partial_\alpha(\rho u_\alpha u_\beta)$ and $u_\beta \partial_\beta(\rho u_\alpha u_\beta)$ are of order $O(u^3)$, which can be neglected. On the other hand, from Eq. (56) we can see $\partial_{t_1} \rho = -\partial_\alpha(\rho u_\alpha)$. Hence, the last term in the above equation is of order $O(u^3)$. Omitting all the terms of order $O(u^3)$, we have

$$\partial_{t_1}(\rho u_\alpha u_\beta) = \partial_\alpha [F_\beta u_\alpha + F_\alpha u_\beta]. \quad (64)$$

Appendix C

The transformation matrix \mathbf{M} for 2D is [28]:

$$\begin{pmatrix} 1 & 1 & 1 & 1 & 1 & 1 & 1 & 1 & 1 \\ -4 & -1 & -1 & -1 & -1 & 2 & 2 & 2 & 2 \\ 4 & -2 & -2 & -2 & -2 & 1 & 1 & 1 & 1 \\ 0 & 1 & 0 & -1 & 0 & 1 & -1 & -1 & 1 \\ 0 & -2 & 0 & 2 & 0 & 1 & -1 & -1 & 1 \\ 0 & 0 & 1 & 0 & -1 & 1 & 1 & -1 & -1 \\ 0 & 0 & -2 & 0 & 2 & 1 & 1 & -1 & -1 \\ 0 & 1 & -1 & 1 & -1 & 0 & 0 & 0 & 0 \\ 0 & 0 & 0 & 0 & 0 & 1 & -1 & 1 & -1 \end{pmatrix}.$$

References

- [1] X.Y. He, S.Y. Chen, R.Y. Zhang, A lattice Boltzmann scheme for incompressible multiphase flow and its application in simulation of Rayleigh–Taylor instability, *J. Comp. Physiol.* 152 (2) (1999) 642–663.
- [2] T. Lee, C.L. Lin, A stable discretization of the lattice Boltzmann equation for simulation of incompressible two-phase flows at high density ratio, *J. Comp. Physiol.* 206 (2005) 16–47.
- [3] T. Lee, P.F. Fischer, Eliminating parasitic currents in the lattice Boltzmann equation method for nonideal gases, *Phys. Rev. E* 74 (2006) 046709.
- [4] L. Amaya-Bower, T. Lee, Single bubble rising dynamics for moderate Reynolds number using Lattice Boltzmann Method, *Comput. Fluids* 39 (2010) 1191–1207.
- [5] T. Lee, L. Liu, Lattice Boltzmann simulations of micron-scale drop impact on dry surfaces, *J. Comp. Physiol.* 229 (2010) 8045–8063.
- [6] L.-S. Luo, Unified theory of the lattice Boltzmann models for nonideal gases, *Phys. Rev. Lett.* 81 (8) (1998) 1618–1621.
- [7] A.K. Gunstensen, D.H. Rothman, S. Zaleski, G. Zanetti, Lattice Boltzmann model of immiscible fluids, *Phys. Rev. A* 43 (8) (1991) 4320–4327.
- [8] D.H. Rothman, J.M. Keller, Immiscible cellular-automaton fluids, *J. Stat. Phys.* 52 (3/4) (1988) 1119–1127.
- [9] H. Huang, J.-J. Huang, X.-Y. Lu, M.C. Sukop, On simulations of high-density ratio flows using color-gradient multiphase lattice Boltzmann models, *Int. J. Mod. Phys. C* 24 (04) (2013) 1350021.
- [10] X. Shan, H. Chen, Lattice Boltzmann model for simulating flows with multiple phases and components, *Phys. Rev. E* 47 (3) (1993) 1815–1819.
- [11] M.C. Sukop, D.T. Thorne, *Lattice Boltzmann Modeling: An Introduction for Geoscientists and Engineers*, Springer, 2006.
- [12] M. Sbragaglia, R. Benzi, L. Biferale, S. Succi, K. Sugiyama, F. Toschi, Generalized lattice Boltzmann method with multirange pseudopotential, *Phys. Rev. E* 75 (2007) 026702.
- [13] H.B. Huang, M. Krafczyk, X.Y. Lu, Forcing term in single-phase and Shan-and-Chen-type multiphase lattice Boltzmann models, *Phys. Rev. E* 84 (2011) 046710.
- [14] K. Sankaranarayanan, X. Shan, I.G. Kevrekidis, S. Sundaresan, Analysis of drag and virtual mass forces in bubbly suspensions using an implicit formulation of the lattice Boltzmann method, *J. Fluid Mech.* 452 (2002) 61–96.
- [15] A. Gupta, R. Kumar, Lattice Boltzmann simulation to study multiple bubble dynamics, *Int. J. Heat Mass Transf.* 51 (21–22) (2008) 5192–5203.
- [16] S. Srivastava, P. Perlekar, J.H.M.t.T. Boonkamp, N. Verma, F. Toschi, Axisymmetric multiphase lattice Boltzmann method, *Phys. Rev. E* 88 (1) (2013) 013309.
- [17] M.R. Swift, E. Orlandini, W.R. Osborn, J.M. Yeomans, Lattice Boltzmann simulations of liquid-gas and binary fluid systems, *Phys. Rev. E* 54 (5) (1996) 5041–5052.
- [18] T. Inamuro, T. Ogata, S. Tajima, N. Konishi, A lattice Boltzmann method for incompressible two-phase flows with large density differences, *J. Comp. Physiol.* 198 (2) (2004) 628–644.
- [19] X. Frank, D. Funfschilling, N. Midoux, H.Z. Li, Bubbles in a viscous liquid: lattice Boltzmann simulation and experimental validation, *J. Fluid Mech.* 546 (2005) 113–122.
- [20] M. Cheng, J. Hua, J. Lou, Simulation of bubble–bubble interaction using a lattice Boltzmann method, *Comput. Fluids* 39 (2) (2010) 260–270.
- [21] H.W. Zheng, C. Shu, Y.T. Chew, A lattice Boltzmann model for multiphase flows with large density ratio, *J. Comp. Physiol.* 218 (1) (2006) 353–371.
- [22] D. Bhaga, M.E. Weber, Bubbles in viscous liquids: shapes, wakes and velocities, *J. Fluid Mech.* 105 (1981) 61–85.
- [23] S. Mukherjee, J. Abraham, Lattice Boltzmann simulations of two-phase flow with high density ratio in axially symmetric geometry, *Phys. Rev. E* 75 (2007) 026701.
- [24] K. Premnath, J. Abraham, Lattice Boltzmann model for axisymmetric multiphase flows, *Phys. Rev. E* 71 (5) (2005) 056706.
- [25] M. McCracken, J. Abraham, Multiple-relaxation-time lattice-Boltzmann model for multiphase flow, *Phys. Rev. E* 71 (3) (2005) 036701.
- [26] J.H. Chao, R.W. Mei, R. Singh, W. Shyy, A filter-based, mass-conserving lattice Boltzmann method for immiscible multiphase flows, *Int. J. Numer. Methods Fluids* 66 (5) (2011) 622–647.
- [27] J. Kim, A continuous surface tension force formulation for diffuse-interface models, *J. Comp. Physiol.* 204 (2) (2005) 784–804.

- [28] P. Lallemand, L.-S. Luo, Theory of the lattice Boltzmann method: dispersion, dissipation, isotropy, Galilean invariance, and stability, *Phys. Rev. E* 61 (6) (2000) 6546–6562.
- [29] G. Son, A numerical method for bubble motion with phase change, *Numer. Heat Transf., Part B, Fundam.* 39 (5) (2001) 509–523.
- [30] J. Hua, J. Lou, Numerical simulation of bubble rising in viscous liquid, *J. Comp. Physiol.* 222 (2) (2007) 769–795.
- [31] D. Jacqmin, Calculation of two-phase Navier–Stokes flows using phase-field modeling, *J. Comp. Physiol.* 155 (1999) 96–127.